Journal of Ship Research, Vol. 63, No. 1, March 2019, pp. 56–68
http://dx.doi.org/10.5957/JOSR.09180054

Challenges in Modeling of Turbulence in the Tip Region of Axial Turbomachines

Yuanchao Li,* Huang Chen,* and **Joseph Katz***

**Johns Hopkins University, Baltimore, MD*

The flow and turbulence in turbomachines are characterized by spatially and temporally nonuniform strain rate fields and tendency to develop partially understood large-scale instabilities. Consequently, the applicability of popular Reynolds stress models in Reynolds-averaged Navier–Stokes simulations of turbomachinery flows is questionable and requires validation under relevant conditions. Experimental studies performed in the Johns Hopkins University optical refractive index–matched facility have investigated the complex flow and turbulence in the blade tip region of several axial turbomachines, including two waterjet pumps and an aviation compressor. The comprehensive databases obtained for different flow conditions and tip geometry using high-resolution particle image velocimetry are used in this article to examine the characteristics of turbulence in the vicinity of the tip leakage vortex (TLV). The results reveal several common features in the spatial distribution of the extremely anisotropic Reynolds stress tensor, suggesting that there are similarities in the mechanisms involved among the different machines. Of the quantities that could be measured accurately, both the local production and mean-flow advection rates appear to govern the evolution of turbulence in the passage. The dissipation rate also appears to be a major factor, but it cannot be measured accurately because of its dependence on motions at small scales that are not resolved by the measurements. The turbulent transport terms are important only in limited cases and locations. The strain rate tensor components, which appear to play primary roles in the production of turbulent kinetic energy (TKE), display common features in the spatial distributions of regions with high contraction, extension, and shear under different conditions. Some but not all of the inhomogeneity and anisotropy in the distributions of Reynolds stresses can be related to the corresponding local production rates. There is disagreement near the TLV core, where the persistent presence of multiple interacting vortices contributes significantly to the elevated TKE there. Lack of a clear functional correlation between the Reynolds stresses and mean strain rates is ubiquitous in all cases, resulting in widely spatially varying positive and negative values for the eddy viscosity. However, surprisingly, results from different machines and conditions have similar spatial distributions of individual stress and strain rate components and, accordingly, the eddy viscosity.

Keywords: turbulence modeling; eddy viscosity

1. Introduction

Modern design processes of turbomachines rely heavily on computational fluid dynamics (CFD) to elucidate the three-dimensional (3D) turbulent flow involved. For decades, Reynolds-averaged Navier–Stokes (RANS) simulations using a variety of

Manuscript received by SNAME headquarters September 22, 2018; accepted December 3, 2018.

Corresponding author: Joseph Katz, katz@jhu.edu

Reynolds stress models have remained the primary approach. However, as pointed out by Lakshminarayana (1986), most popular turbulence models are derived/calibrated based on results obtained in simple flows, raising questions about their applicability to complex turbomachinery flows. The impact of different models on flow predictions has already been examined by numerous researchers (Liu et al. 2008), too many to summarize here. Some issues associated with popular turbulence models include, e.g., the required tuning of empirical constants (Denton 1997), generation of negative normal stresses (Moore & Moore 1999), the stagnation point anomaly (Durbin 1996), and the prevalence of anisotropic turbulence in contrast to the predictions by the widely used k-ε model (Liu et al. 2008). Techniques that resolve part of turbulent motions, such as large eddy simulations, might solve some of these issues, but their use is still limited, especially for design purposes, and they also raise questions about modeling sub-grid stresses. Hence, careful validation of RANS predictions of turbomachinery flows by experimental data remains critical (Horlock & Denton 2005; Denton 2010). Although substantial amount of data is available on the overall performance of different machines, there is very limited information about the flow and Reynolds stresses in them (Peacock 1983; Inoue & Kuroumaru 1989; Goto 1992; Jang et al. 2005; Yu & Liu 2007).

To this end, systematic experimental studies performed at the Johns Hopkins University (JHU) in recent years have examined the flow structure in several axial turbomachines, including two waterjet pumps (Wu et al. 2011a, 2011b; Miorini et al. 2012; Wu et al. 2012; Tan et al. 2015a, 2015b) and an aviation compressor (Tan et al. 2015a, 2015b; Li et al. 2017). The experiments were performed in a refractive index–matched facility described briefly in the next section. The comprehensive databases have been used to elucidate mechanisms affecting the complex turbulence structures, focusing on the tip region of the rotor blade, where the flow is dominated by the presence of backward leakage from the pressure to the suction side (SS) of the blade across the tip gap, and the tip leakage vortex (TLV) (Wu et al. 2012; Li et al. 2017). They show that the turbulent kinetic energy (TKE) is high in the shear layer separating the backward leakage flow and the forward main passage flow under it, around the TLV center, and in the region of endwall boundary layer separation, where the leakage flow meets the main passage flow. Some of the causes for the anisotropic and inhomogeneous distributions of Reynolds stresses are attributed to variability in the corresponding turbulence production rates, such as high positive turbulence production rates in regions of mean flow contraction and shear, and negative production in regions of extension. The current article generalizes the discussion by examining the structure of Reynolds stresses in several axial turbomachines at different operating conditions, focusing on common features that appear in many of them. The results demonstrate the fundamental challenges in modeling Reynolds stresses in flows dominated by non-equilibrium conditions, i.e., when the local Reynolds stresses are affected by the time history of turbulence development and are not necessarily correlated with the local mean strain rate tensor. Such correlation is fundamental to all the popular eddy viscosity–based models (Pope 2000). As shown in this article, in spite of substantial differences in blade loading and time history, some of the characteristic features of the turbulence persist, including the spatially varying distributions of eddy viscosity. These trends might guide the development of more adequate Reynolds stress models.

2. Experimental setup

All the measurements have been performed in the JHU refractive index–matched facility, which has already been described in multiple references (Wu et al. 2011a, 2011b; Miorini et al. 2012; Wu et al. 2012; Tan et al. 2015a, 2015b; Chen et al. 2017; Li et al. 2017). A sketch of this liquid test loop with two of the turbomachines involved is provided in Figs. 1 and 2A, B. The casing and blades of these machines are made of transparent acrylic, which has the same refractive index (1.49) as the liquid, a concentrated aqueous solution of sodium iodide. Several large flat outer casing surfaces facilitate unobstructed observations from any desired angle, allowing for implementation of particle image velocimetry (PIV) at any location. To date, tip leakage flows have been systematically studied in two axial waterjet pumps, referred to as AxWJ-1 (Miorini et al. 2012; Wu et al. 2012) and AxWJ-2 (Tan et al. 2015a, 2015b), and an aviation compressor, derived from the first 1.5 stages of the low-speed axial compressor (LSAC) facility at NASA Glenn (Hah et al. 2014, 2015; Tan et al. 2014, 2015a, 2015b). Earlier work investigated the turbulence generated because of wake–wake and wake–blade interactions (Soranna et al. 2006, 2010) at mid-span. These machines are designed/derived for different applications, and accordingly, their blade geometry and numbers as well as operating conditions differ substantially. A brief comparison of the rotor blade geometric parameters for two waterjet pumps and the NASA compressor is provided in Table 1. The measurements have been performed at 900 rpm for the two waterjet pumps and 480 rpm for the compressor, resulting in the characteristic Reynolds numbers based on the blade chord length listed in Table 1. In this study, the machine performance is characterized by 1) the *flow coefficient*, $\varphi = (Q/A)/U_T$, where Q is the volumetric flow rate, A is the throughflow area, and U_T is the rotor blade tip speed, and 2) the *head-rise coefficient*, $\psi = \Delta p/(.5\ \rho\ U_T^2)$, where Δp is the total pressure rise across the entire machine. Note that other definitions are used in earlier articles describing waterjet pumps (Wu et al. 2012), namely, $\varphi^* = Q(\Omega/2\pi)^{-1}D^{-3}$ and $\psi^* = (\Delta p/\rho)(\Omega/2\pi)^{-2}D^{-2}$, where Ω is the rotor angular velocity and D is the casing inner diameter. The operating conditions at which the PIV measurements are performed in the axial waterjet pumps correspond to their best efficiency points (BEPs), $\varphi = .14$ for AxWJ-1 and $\varphi = .32$ for AxWJ-2. The compressor has been studied using two sets of similar blades with significantly different tip gaps (Table 1), each at two operating conditions: $\varphi = .35$, representing a high flow rate near the peak efficiency point, and $\varphi = .25$, representing pre-stall conditions. All the data used in this study have been obtained with smooth endwalls.

All the data presented in this article has been obtained using Stereo-PIV (SPIV), details of which can be found in, e.g., Li et al. (2017). In all cases, silver-coated hollow spherical particles with a mean diameter of 13 μm and a specific gravity of 1.6 are used as flow tracers. The sample planes are aligned in the meridional (z-r) directions, and images are recorded by a pair of PCO.2000 CCD (Manufactured by PCO-Tech Inc, Kelheim, Germany) 2048×2048-pixels cameras aligned symmetrically on both sides of the laser sheet, with the lenses inclined by the Scheimpflug angles. The cameras and lasers are synchronized with the rotor orientation using a shaft encoder and a time-delay controller. The typical time interval between exposures is 20 μs. This PIV system is calibrated following the two-step procedure described by Wieneke (2005),

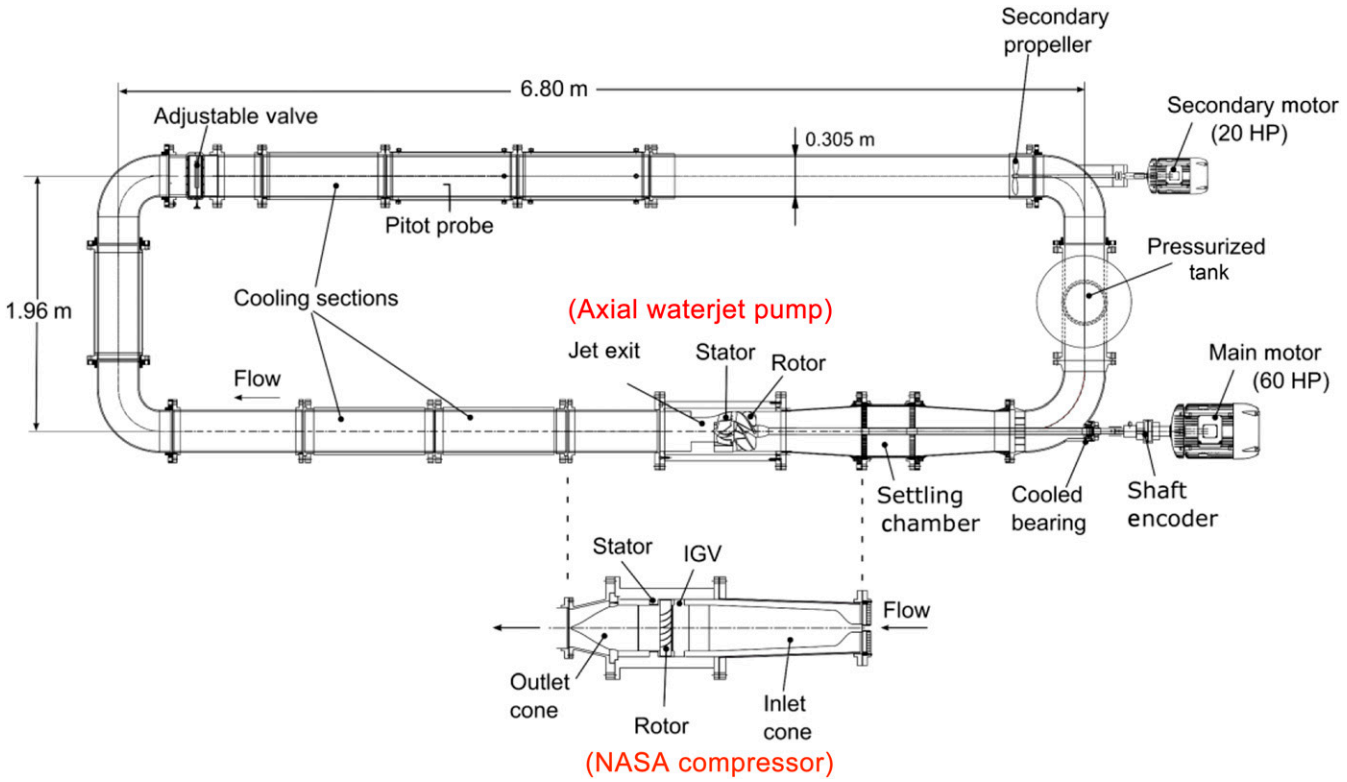

Fig. 1 A sketch of the JHU refractive index–matched test loop facilitating the waterjet pump (AxWJ-2) and the axial compressor

as detailed in Li et al. (2016). The PIV images are pre-processed by subtracting the background and enhanced using a modified histogram equalization algorithm (Roth & Katz 2001). Then, velocity vectors are calculated by multi-pass cross-correlations using the commercial software LaVision DaVis (Software provided by LaVision GmbH, Göttingen, Germany). Typical vector spacings in the data included in this article are .244 mm for the AxWJ-1 pump, .107 mm for the AxWJ-2 pump, and .161 mm for the compressor. The corresponding fields of view are 14×26, 12×17, and 21×29 mm^2, respectively. Data consisting of all three velocity components have been recorded in numerous planes. However, for the compressor (Chen et al. 2017; Li et al. 2017) and AxWJ-1 (Wu et al. 2011a, 2011b), at selected locations, data are also recorded in a series of multiple closely spaced planes, separated by a distance comparable to the vector spacing. For these volumes, all the components of the time-averaged stain-rate tensor and vorticity are known, including those involving out-of-plane gradients ($\partial/\partial\theta$) (Wu et al. 2011a, 2011b, 2012; Chen et al. 2017; Li et al. 2017). To ensure convergence of the ensemble statistics, at least 1000 and 2500 realizations are recorded at the same location and condition for the waterjet pumps and the compressor, respectively. The uncertainty level in instantaneous velocity is about 2% (Wu et al.

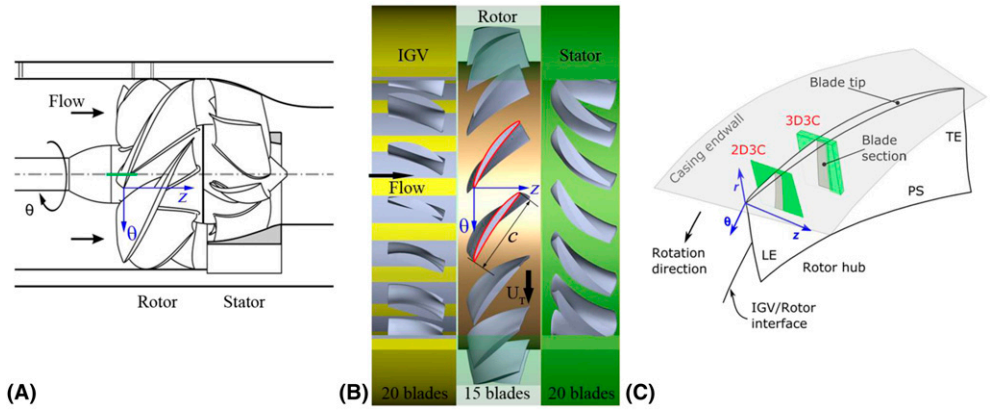

Fig. 2 Sketches show (A) the blade rows of the AxWJ-2 pump, (B) the axial compressor, and (C) typical PIV sampling domains in the tip region of the compressor rotor blade

Table 1 Comparisons of the rotor geometric parameters for axial turbomachines

	AxWJ-1 pump	AxWJ-2 pump	NASA compressor
Number of blade rows	2	2	3
Rotor blade numbers (N_R)	7	6	15
Stator blade numbers (N_S)	11	8	20
Casing inner diameter (D) (mm)	304.8	306.2	457.2
Rotor diameter (D_R) (mm)	303.4	303.8	456, 453.6
Tip chord length (c) (mm)	267.2	274.3	102.6
Tip axial chord (c_A) (mm)	74.5	127.4	53.5
Tip stagger angle (γ) (deg)	16.2	27.7	58.6
Tip solidity	1.96	1.72	1.08
Nominal tip clearance (mm)	.7	.7	.64, 1.8
Measured tip clearance (mm)	1.0	.9	.5, 2.4
Shaft speed (Ω) (rad/s) {RPM}	94.2 {900}	94.2 {900}	50.27 {480}
Tip speed (U_T) (m/s)	14.4	14.32	11.47
Reynolds number ($Re_c = U_T c/\nu$)	3.5×10^6	3.6×10^6	1.07×10^6

2011a; Wu et al. 2011b; Roth & Katz 2001), and ensemble averaging reduces the uncertainty in mean velocity to about $1/\sqrt{N}$ ($N = 1000$ or 2500) of the instantaneous values. The uncertainty level in Reynolds stresses and TKE is about 5%. Further derived terms, e.g., the turbulence production rate, can have an uncertainty level about 10-15% (Soranna et al. 2008). One should note that although the same facility can be used for cavitation tests (e.g., Tan et al. 2015b), all the PIV data used in this paper are measured with a cavitation-free condition, i.e., with increased mean pressure over the entire facility.

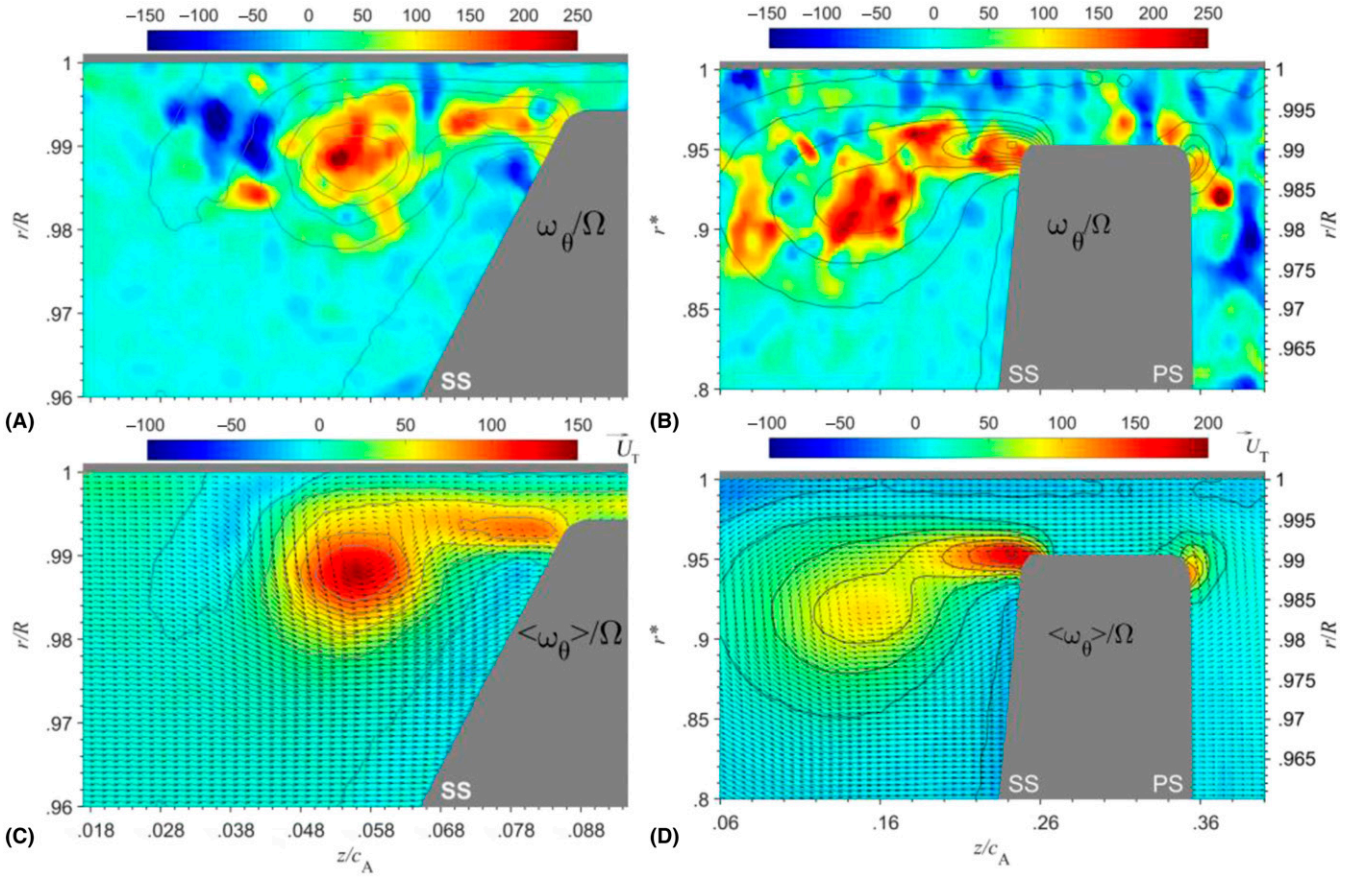

Fig. 3 Sample distributions of (A, B) instantaneous (ω_θ/Ω) and (C, D) ensemble-averaged ($\langle\omega_\theta\rangle/\Omega$) vorticity for (A, C) the AxWJ-2 pump and (B, D) the axial compressor. Vectors in (C, D) represent the ensemble-averaged in-plane velocity field ($\langle u_z\rangle/U_T$, $\langle u_r\rangle/U_T$), diluted by 2:1 in the z-direction for clarity

To present the data in a consistent manner, a cylindrical coordinate system (r, θ, z) is adopted for all the machines, as shown in Figs. 2B, C. The origin of this system is located at the center of the shaft, with $z = 0$ and $\theta = 0$ coinciding with the blade tip leading edge. In all cases, the z-coordinate is normalized using the blade tip axial chord length c_A provided in Table 1. However, in accordance with previous publications, the r-coordinate is scaled differently for the pumps and compressor, the former using r/R, where R is the radius of the casing inner surface, and the latter using $r^* = (r - r_{hub})/L$, where L is the distance from the hub to the casing endwall. To enable adequate comparisons, the corresponding r/R for the compressor is also provided on the right-hand side of some figures. All the data analyses discussed in this article were performed in a rotating reference frame, denoted by *.

3. Results

3.1. Common features in the dynamics of turbulence in the tip regions

Figure 3 provides sample distributions of the instantaneous circumferential vorticity (ω_θ/Ω) for the AxWJ-2 pump (Fig. 3A) and the compressor (Fig. 3B). The former only displays the SS of the rotor blade tip, but the latter covers both the SS and the pressure side (PS). As discussed in multiple previous publications (Wu et al. 2011a, 2011b; Miorini et al. 2012; Wu et al. 2012; Tan et al. 2015a, 2015b; Li et al. 2016), in instantaneous realizations, the tip region of all the present axial turbomachines contains multiple interacting vortices. The corresponding ensemble-averaged vorticity contours, $\langle\omega_\theta\rangle/\Omega$, presented in Figs. 3C, D, where $\langle\cdot\rangle$ indicates ensemble averaging, display several characteristic mean vortical structures. The most prominent are the TLV, a shear layer connecting the TLV to the blade SS tip corner, and a layer with opposite sign vorticity, which is generated as the endwall boundary layer separates when the backward leakage flow meets the main passage flow upstream of the TLV, e.g., at $z/c_A \sim .044$ and $r/R = 1.0$ in Fig. 3c).

Figure 4 shows the samples of TKE distributions, $k = .5(\langle u_z'^2\rangle + \langle u_r'^2\rangle + \langle u_\theta'^2\rangle)$, where the prime denotes fluctuating variables, i.e., $u_i' = u_i - \langle u_i\rangle$. In these plots, s/c indicates the point where the PIV laser sheet intersects the blade chord. Evidently, in all the machines and operating conditions, the TKE elevated in three distinct regions. First, the TKE has a peak in the TLV center. As demonstrated in Miorini et al. (2012), about 40% of the contribution to this peak is associated with variations in the location and strength of the aforementioned large-scale vortices. Second, the TKE is persistently elevated in the shear layer separating the backward leakage flow and the forward main passage flow below it, which connects the SS tip corner to the TLV. Third, the turbulence is high in the region of endwall boundary layer separation upstream of the TLV. In most cases (Figs. 4A–D), this layer is subsequently entrained radially inward by the TLV. The two wide-gap samples (Figs. 4E, F), where the TLV is located too far to entrain the separated layer (Li et al. 2016), are the only exceptions. For the latter case, the turbulence level increases substantially over the entire tip region with decreasing flow rate on both sides of the blade. Figure 4F represents pre-stall conditions, where large-scale backflow vortices, which form radially inward from the TLV, propagate from the mid-chord SS of one blade toward the PS of the adjacent blade. The elevated turbulence on the PS in Fig. 4F represents the effect of these structures along with those of fragmented remnants of a previous TLV. Because of the wide tip clearance, the elevated PS turbulence is entrained/ingested to the SS by the leakage flow, increasing the turbulence levels there, and

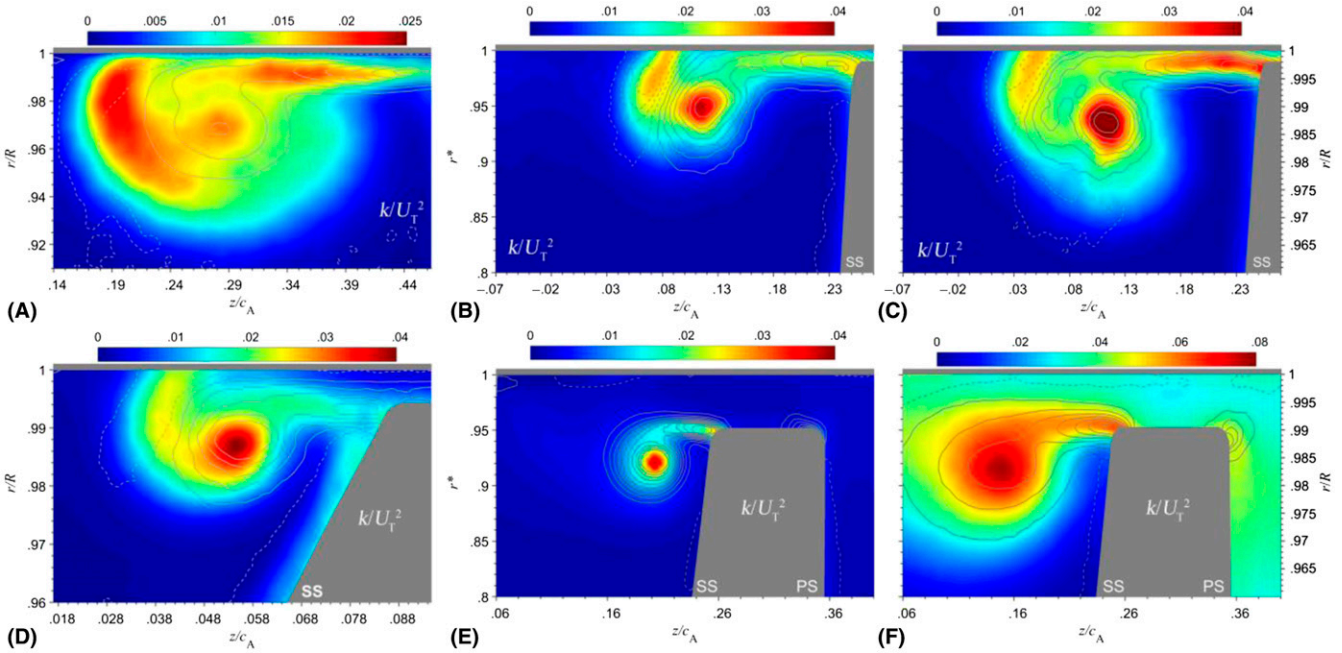

Fig. 4 Characteristic distributions of TKE (k/U_T^2) for the (A) AxWJ-1 pump, $s/c = .67$ near the BEP; (B, C) compressor with a small tip gap at $s/c = .44$ for (B) $\varphi = .35$ and (C) $\varphi = .25$; (D) AxWJ-2 pump at $s/c = .13$ near the BEP; (E, F) compressor with a large tip gap at $s/c = .44$ for (E) $\varphi = .35$, and (F) $\varphi = .25$. The black contour lines represent the distributions of $\langle\omega_\theta\rangle/\Omega$, with dashed lines showing negative values

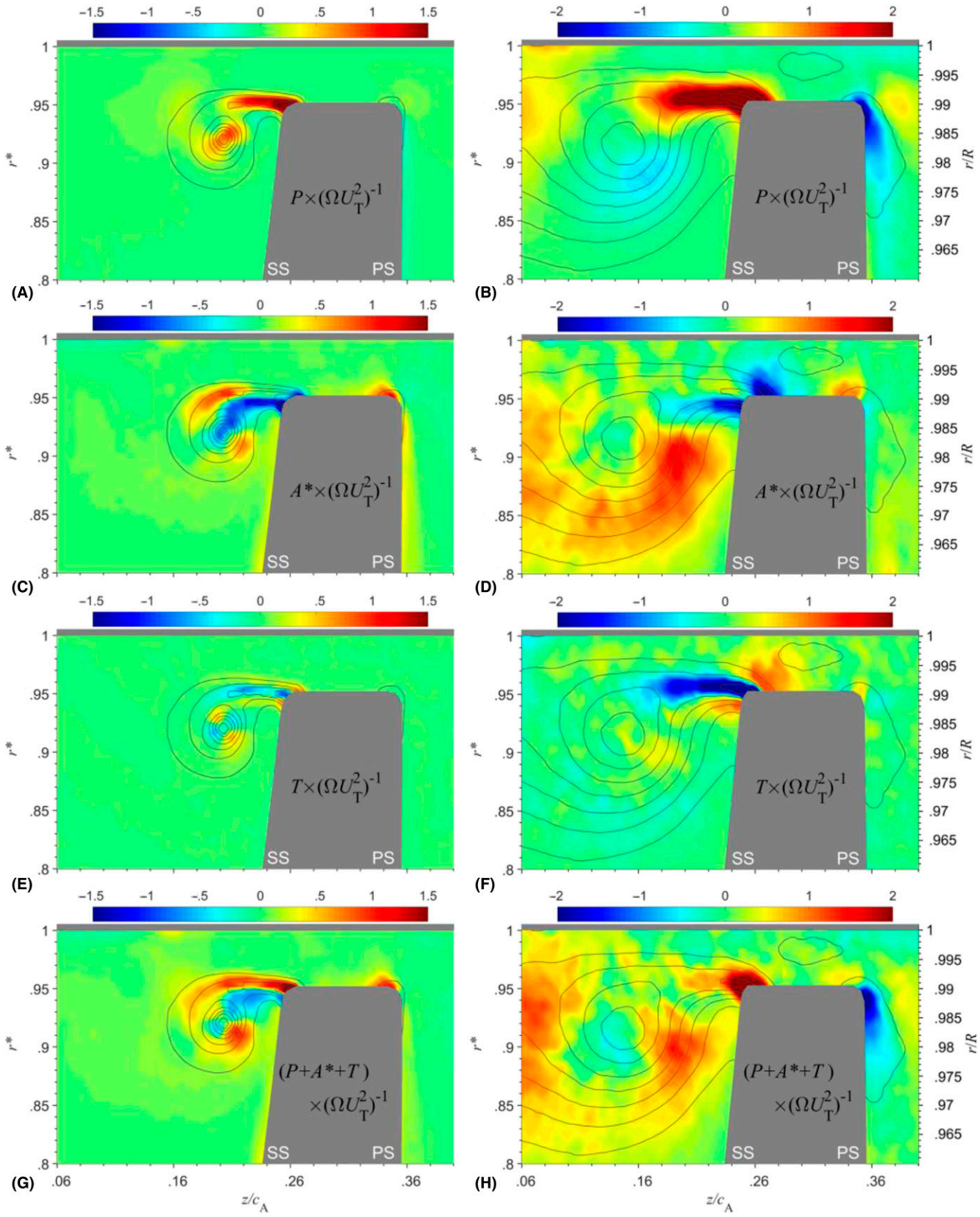

Fig. 5 Sample distributions of (A, B) TKE production rates, $P\times(\Omega U_T^2)^{-1}$; (C, D) advection rates by mean flow, $A^*\times(\Omega U_T^2)^{-1}$; (E, F) turbulence transport rate, $T\times(\Omega U_T^2)^{-1}$; and (G, H) their combined effects, $(P + A^* + T)\times(\Omega U_T^2)^{-1}$, for the compressor at (left column) $\varphi = .35$ and (right column) $\varphi = .25$. The black contour lines represent the corresponding TKE levels

triggering the formation of new BFVs (Li et al. 2016; Chen et al. 2017).

The aforementioned common features in the TKE distributions can be partly attributed to the local production process, i.e., to the interactions between Reynolds stress and mean strain rate fields, which act as sources for new turbulence. The total production rate of TKE is as follows:

$$P = -\langle u_i' u_j' \rangle \partial_j \langle u_i \rangle = -\langle u_i' u_j' \rangle S_{ij}, \tag{1}$$

where S_{ij} is the mean strain rate, and i, j are tensor indices and double indices indicating summation. Sample distributions of TKE production rates for the compressor with a large tip gap at high and low flow rates are provided in Figs. 5A, B, respectively. For both, P has high positive values in the shear layer, consistent with the elevated TKE levels there. However, trends are different near the TLV center, where positive high production is observed for $\varphi = .35$ but not for $\varphi = .25$. As discussed later, the reason for this flow-rate dependence is associated with the production rate of $\langle u_z'^2 \rangle$. The values of P are also elevated in the region where the endwall boundary layer separates ($z/c_A \sim .07$, $r^* > .9$), evident in this sample for $\varphi = .25$, but not for $\varphi = .35$. In other cases involving narrow gaps and entrainment of the separated endwall boundary layer, the production rate has a high peak near the separation point (Wu et al. 2012). In general, persistent trends include high positive production

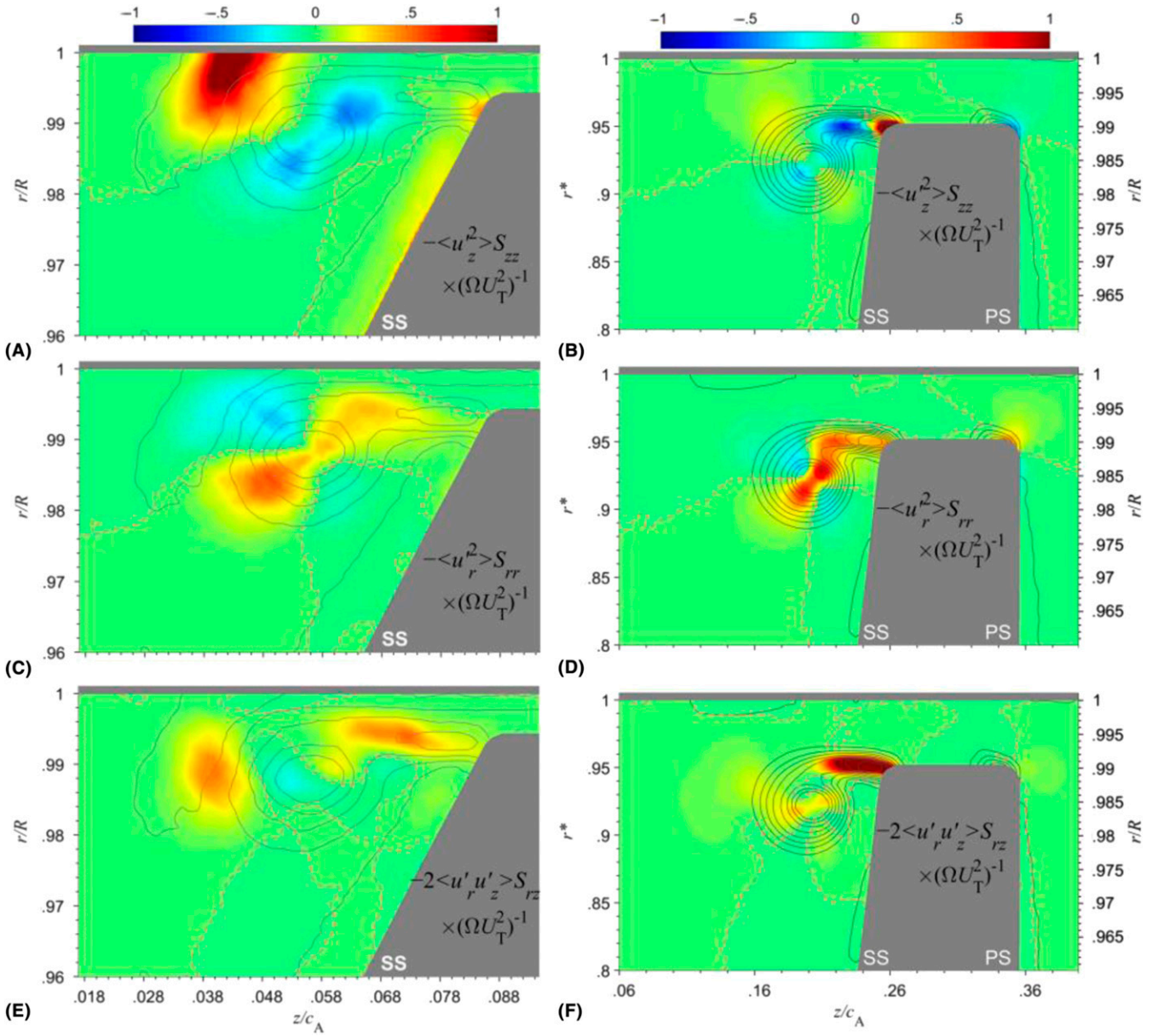

Fig. 6 Dominant production rate terms associated with (A, B) axial contraction/stretching $(-\langle u_z'^2 \rangle S_{zz} \times (\Omega U_T^2)^{-1})$, (C, D) radial contraction/stretching $(-\langle u_r'^2 \rangle S_{rr} \times (\Omega U_T^2)^{-1})$, and (E, F) shear effects $(-2\langle u_z' u_r' \rangle S_{rz} \times (\Omega U_T^2)^{-1})$. Left column (A, C, E): AxWJ-2 pump; and right column (B, D, F): axial compressor. The red dashed lines indicate the locations of zero values. The gray contour lines correspond to $\langle \omega_\theta \rangle / \Omega$

in the shear layer and in the endwall separated region. One should also note that there are regions with negative production rate, i.e., P acts as a "sink" for turbulence, which indicates the existence of a non-equilibrium condition.

Figure 6 provides sample distributions of the dominant terms contributing to P for the AxWJ-2 pump (left column) and the compressor (right column) near their design points. Several common features are evident: First, common regions with positive axial contraction term, $-\langle u_z'^2\rangle S_{zz}$ (Figs. 6A, B), are located around the points of endwall boundary layer separation, and near the SS tip corner. The former is very high in AxWJ-2 (Fig. 6A), and the latter, in the compressor (Fig. 6B). Second, near the TLV center, $-\langle u_z'^2\rangle S_{zz}$ (Figs. 6A, B) and the radial contraction term, $-\langle u_r'^2\rangle S_{rr}$ (Figs. 6C, D), show what appears to be diagonal four-quadrant patterns with opposite signs. This pattern is caused by the opposite signs in the corresponding strain rates; i.e., flow stretching in one direction co-occurs with contraction in the perpendicular direction. Third, the shear production rate term, $-2\langle u_r' u_z'\rangle S_{rz}$ (Figs. 6E, F), commonly has elevated positive values in the shear layer and in a region between the TLV center and the endwall separation point. Similar spatial patterns in the distributions of these three dominant production rate terms can also be observed in the compressor at pre-stall condition (not shown) and for the AxWJ-1 pump (Miorini et al. 2012).

Other terms affecting the evolution of TKE, as indicated by the TKE transport equation:

$$\frac{\partial k}{\partial t} = P + A^* + M + T + \Pi - \varepsilon, \tag{2}$$

include the mean flow advection (A^*), viscous diffusion (M), turbulent diffusion (T), pressure diffusion (Π), and dissipation rate (ε) (Lakshminarayana 1996; Pope 2000). Examination of these terms might explain some of the inconsistency between the distributions of TKE and its production rate, e.g., regions under the TLV center in Fig. 5B. Li et al. (2017) show that A^* and ε are of the similar magnitude as P, and that M and T are typically significantly smaller. Because of the high turbulence levels and resulting very small Kolmogorov scales, the spatial resolutions in all the current measurements cannot provide accurate values for ε directly (Luznik et al. 2007; Delafosse et al. 2011; Xu & Chen 2013). Furthermore, Π cannot be calculated based on the presently available snapshots of SPIV data, although techniques based on 3D time-resolved PIV measurements have already been developed in recent years for calculating the pressure in turbulent flows (Liu & Katz 2006; Charonko et al. 2010; de Kat & Ganapathisubramani 2013; Liu & Katz 2013; Zhang et al. 2017). Hence, the discussion on effects of the transport terms focuses on the mean advection rate, $A^* = (U_z\partial_z k + U_r\partial_r k + U_\theta^* r^{-1}\partial_\theta k)$, presented in Figs. 5C, D. Note that A^* depends on the choice of the reference frame. As expected, A^* is elevated in regions of large spatial gradients in k. In certain areas, the sign of A^* is opposite to that of P, e.g., in the shear layer and near the TLV center, indicating transport of turbulence away from regions of high production by the mean flow. The distributions of T are presented in Figs. 5E, F. This term is smaller than P or A^* but non-negligible at $\varphi = .35$. However, it has a significant impact on the shear layer and near the blade SS tip corner at $\varphi = .25$. The combined effect of these terms, i.e., $(P + A^* + T)$, presented in Figs. 5G, H, still show regions with high positive or negative values, except for the periodic unsteadiness associated with the inlet guide vane wakes, which is not negligible (Soranna et al. 2006, 2010), in the rotor reference frame, $\partial k/\partial t \approx 0$, i.e., $P + A^* + M + T + \Pi - \varepsilon \approx 0$. Hence, $(P + A^* + T)$ should be balanced by Π–ε. This conclusion leads to two observations: First, since $(P + A^* + T)$ is small near the TLV center for both flow rates, in contrast to the elevated TKE there, the dissipation rate is also expected to be low, assuming a

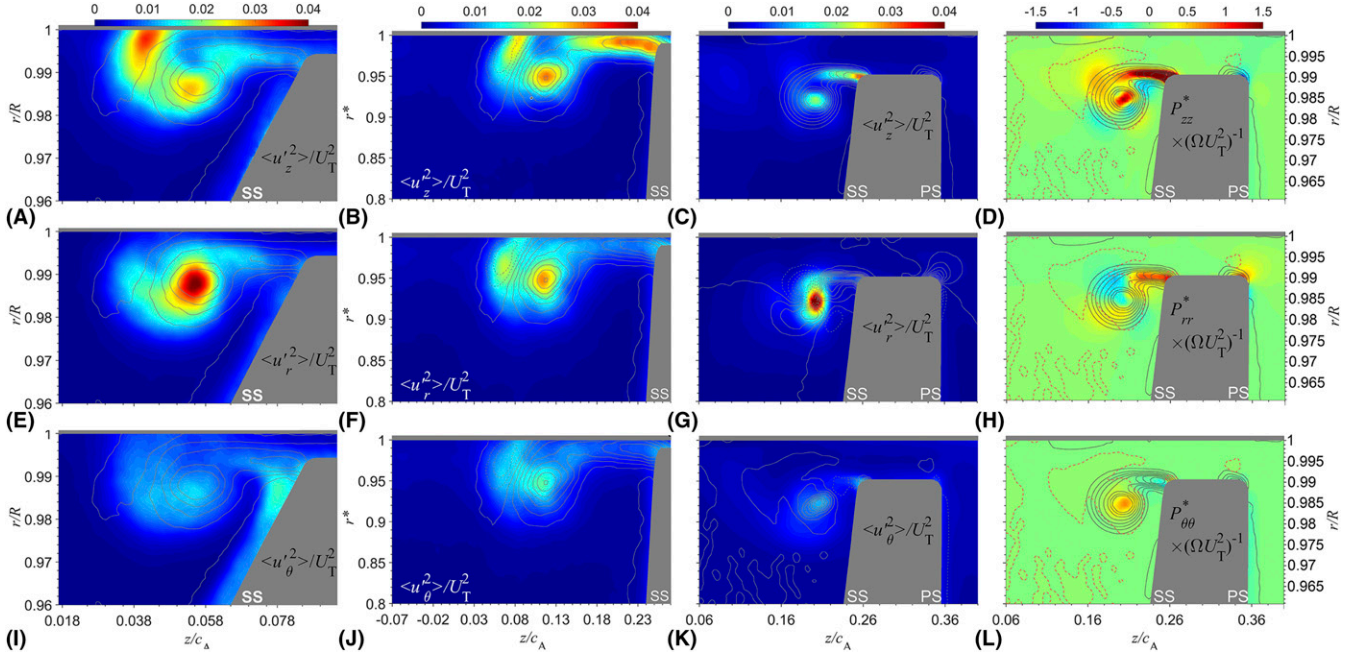

Fig. 7 Sample distributions of Reynolds normal stresses: (A, B, C) $\langle u_z'^2\rangle/\Omega U_T^2$, (E, F, G) $\langle u_r'^2\rangle/\Omega U_T^2$, and (I, J, K) $\langle u_\theta'^2\rangle/U_T^2$ for (A, E, I) the AxWJ-2 pump at its BEP, and the axial compressor with (B, F, J) a narrow tip gap and (C, G, K) a wide tip gap at $\varphi = .35$; (D, H, L) distributions of the corresponding production rate terms: (D) $P_{zz}^* \times (\Omega U_T^2)^{-1}$, (H) $P_{rr}^* \times (\Omega U_T^2)^{-1}$, and (L) $P_{\theta\theta}^* \times (\Omega U_T^2)^{-1}$ for the wide gap compressor, with red dashed lines indicating the locations of zero values. The gray contour lines correspond to $\langle\omega_\theta\rangle/\Omega$

small pressure diffusion term there. As postulated in Wu et al. (2012) based on the AxWJ-1 data, low dissipation rate in a region of elevated TKE could be associated with the unsteady motions of large-scale vortices, which contribute to the TKE, but not-necessarily to dissipation, which is dominated by small scale shear. Second, at the high flow rate, the values of $(P + A^* + T)$ are negative in the lower part of the shear layer, which cannot be balanced by the inherently positive ε, suggesting that the pressure diffusion might play an important role there. Time-resolved 3D measurements planned for the future will quantify the mechanisms involved.

3.2. Anisotropy of Reynolds stresses

This subsection focuses on common features in the spatial distribution of the Reynolds stress tensor. Figure 7 shows the sample data for the Reynolds normal stresses ($\langle u_z'^2\rangle$, $\langle u_r'^2\rangle$, $\langle u_\theta'^2\rangle$) near the BEPs of several machines. The corresponding production rate terms in a rotating reference frame are calculated using the following equations:

$$P_{zz}^* = -2\left[\begin{array}{l}\langle u_r'^2\rangle\dfrac{\partial\langle u_z\rangle}{\partial z} + \langle u_z'u_r'\rangle\dfrac{\partial\langle u_z\rangle}{\partial r}\\ +\langle u_z'u_\theta'\rangle\dfrac{1}{r}\dfrac{\partial\langle u_z\rangle}{\partial\theta}\end{array}\right], \tag{3}$$

$$P_{rr}^* = -2\left[\begin{array}{l}\langle u_z'u_r'\rangle\dfrac{\partial\langle u_r\rangle}{\partial z} + \langle u_r'^2\rangle\dfrac{\partial\langle u_r\rangle}{\partial r}\\ +\langle u_r'u_\theta'\rangle\left(\dfrac{1}{r}\dfrac{\partial\langle u_r\rangle}{\partial\theta} - \dfrac{\langle u_\theta^*\rangle}{r}\right)\\ -\langle u_r'u_\theta'\rangle\dfrac{\langle u_\theta^*\rangle}{r}\end{array}\right] + 4\Omega\langle u_r'u_\theta'\rangle, \tag{4}$$

$$P_{\theta\theta}^* = -2\left[\begin{array}{l}\langle u_z'u_\theta'\rangle\dfrac{\partial\langle u_\theta^*\rangle}{\partial z} + \langle u_r'u_\theta'\rangle\dfrac{\partial\langle u_\theta^*\rangle}{\partial r}\\ +\langle u_\theta'^2\rangle\left(\dfrac{1}{r}\dfrac{\partial\langle u_\theta^*\rangle}{\partial\theta} + \dfrac{\langle u_r\rangle}{r}\right)\\ +\langle u_r'u_\theta'\rangle\dfrac{\langle u_\theta^*\rangle}{r}\end{array}\right] - 4\Omega\langle u_r'u_\theta'\rangle. \tag{5}$$

Results for the compressor are provided in Figs. 7D, H, L, as examples for characteristic trends. Some common and distinct patterns in the spatial distributions of these stress and production components can be summarized as follows:

1) In all cases, $\langle u_z'^2\rangle$ is large near the TLV center and in the shear layer. When the tip clearance is small (Figs. 7A, B),

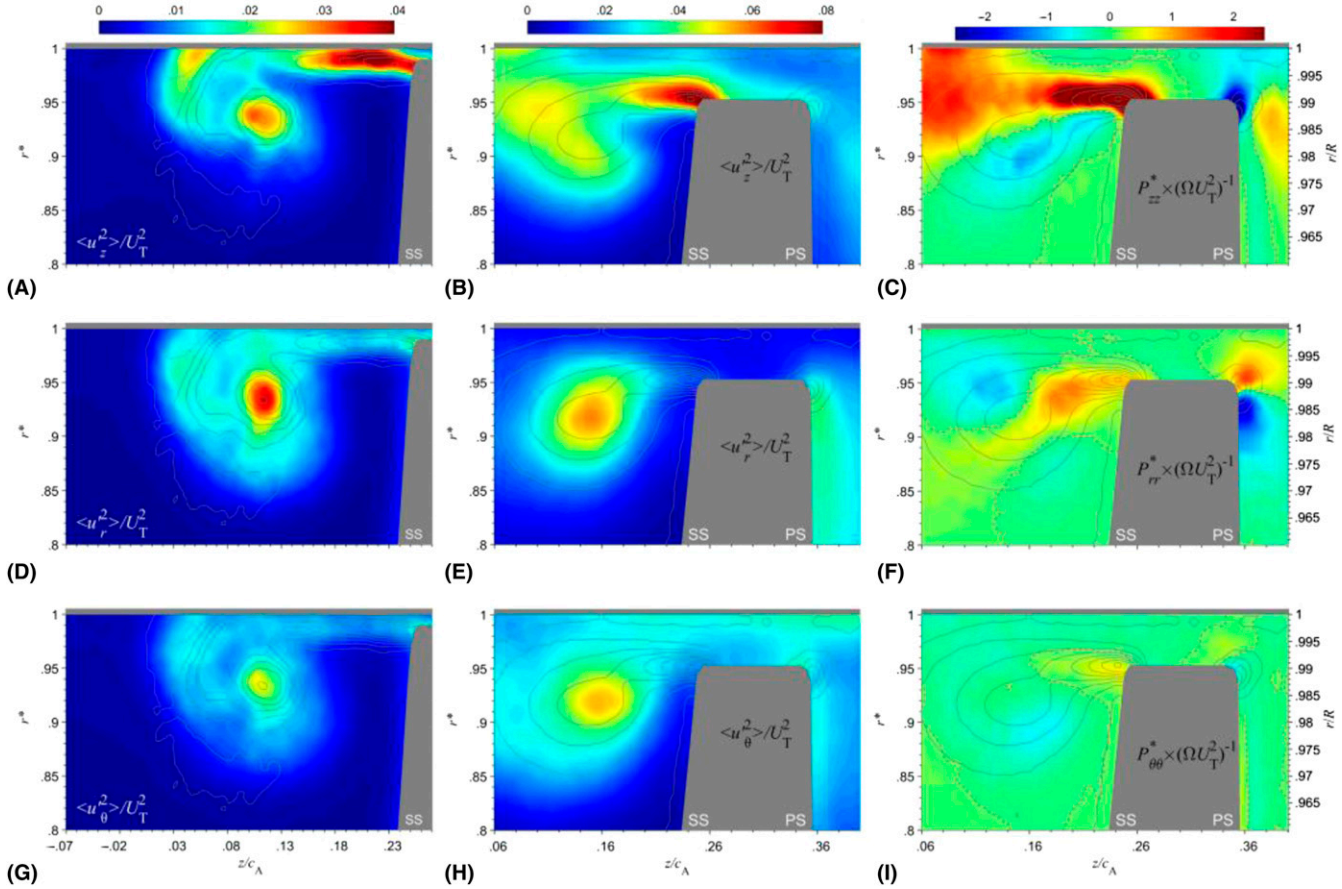

Fig. 8 Sample distributions of Reynolds normal stresses: (A, B) $\langle u_z'^2\rangle/U_T^2$, (D, E) $\langle u_r'^2\rangle/U_T^2$, and (G, H) $\langle u_\theta'^2\rangle/U_T^2$ for the compressor with (A, D, G) a narrow tip gap and (B, E, H) a wide tip gap at $\varphi = .25$ (C, F, I). Distributions of the corresponding production rate terms (C) $P_{zz}^* \times (\Omega U_T^2)^{-1}$, (F) $P_{zz}^* \times (\Omega U_T^2)^{-1}$, and (I) $P_{\theta\theta}^* \times (\Omega U_T^2)^{-1}$ for the wide gap compressor, with red dashed lines indicating the locations of zero values. The gray contour lines correspond to $\langle\omega_\theta\rangle/\Omega$

$\langle u_z'^2 \rangle$ is also elevated in the endwall separated layer. By contrast, for the cases with a large tip gap (Fig. 7C), $\langle u_z'^2 \rangle$ is only slightly higher than the surrounding level, presumably because of a weaker influence of the TLV.

2) Among all machines, $\langle u_r'^2 \rangle$ peaks in the TLV center. For AxWJ-2 (Fig. 7E) and the compressor with a wide gap (Fig. 7G), $\langle u_r'^2 \rangle$ dominates near the TLV center, consistent with the result in Lakshminarayana et al. (1982). For the compressor with a narrow gap, $\langle u_r'^2 \rangle$ is close but slightly lower than $\langle u_z'^2 \rangle$. Conversely, for all cases, $\langle u_r'^2 \rangle$ is smaller than $\langle u_z'^2 \rangle$ in the shear layer and in the endwall separated regions.
3) Although they peak in the same regions as the other components, the magnitudes of $\langle u_\theta'^2 \rangle$ (Figs. 7I–K) are consistently significantly lower than those of the other components for the present three cases. However, this trend is not universal. For example, in AxWJ-1 (Wu et al. 2012), $\langle u_\theta'^2 \rangle$ is comparable to $\langle u_z'^2 \rangle$, and both are larger than $\langle u_r'^2 \rangle$.
4) As shown in previous publications (Wu et al. 2012; Li et al. 2017), the spatial variability and anisotropy of these stresses can be partly explained by examining the corresponding production rates. Figure 7 provides comparative data for the compressor with a wide tip clearance. As is evident, in Fig. 7D, P_{zz}^* is positive and high in the shear layer and near the TLV center, consistent with the locations of $\langle u_z'^2 \rangle$ peaks in Fig. 7C. The values of $P_{\theta\theta}^*$ (Fig. 7L) are positive but relatively small near the vortex center, also in agreement with the magnitudes of $\langle u_\theta'^2 \rangle$ there. However, there are also inconsistent trends. For example, P_{rr}^* is slightly negative in the TLV center (Fig. 7H), in contrast to the high $\langle u_r'^2 \rangle$ there. Hence, the entire set of potential contributors, including transport and dissipation, must be considered to explain this phenomenon.

Sample Reynolds normal stress components for the compressor at pre-stall conditions are provided in Fig. 8 for the narrow gap (left column) and the wide gap (middle column). The corresponding production rate terms for the latter are shown in the right column. Overall, all the stress components are higher than those at high flow rates for the same machine (note the differences in scale). Some trends occur for both cases, such as the large values of $\langle u_z'^2 \rangle$ in the shear layer, close to the blade SS tip corner, the peak of $\langle u_r'^2 \rangle$ in the TLV center, and the lower, but distinct maximum of $\langle u_\theta'^2 \rangle$ near the vortex center. In terms of clearance size effects, for the narrow gap, all the normal stress components are elevated in the endwall boundary layer separation region, with $\langle u_z'^2 \rangle$ being the largest and $\langle u_\theta'^2 \rangle$ the smallest. For the wide gap, all the peaks are broader, and there is no distinct $\langle u_z'^2 \rangle$ peak near the vortex center. Along the PS, as one would expect (Soranna et al. 2008), the stress components parallel to the surface are elevated, whereas the component normal to the surface ($\langle u_z'^2 \rangle$) is suppressed. The same trend occurs in the tip gap, but here, $\langle u_r'^2 \rangle$ is suppressed. The high positive P_{zz}^* (Fig. 8C) in the shear layer and in the endwall separation regions are consistent with the elevated $\langle u_z'^2 \rangle$ there. However, the negative P_{zz}^* near the blade PS tip corner and under the TLV center are inconsistent with the high stress there, indicating that transport and inter-component energy transfer might play significant roles. Furthermore, around the TLV center, the partially positive and negative values of P_{rr}^* (Fig. 8F) do not coincide with the broad area with high $\langle u_r'^2 \rangle$. Trends in the shear layer and along the PS for this component also do not agree. Figure 8I shows that $P_{\theta\theta}^*$ is lower than the other production terms and is negative around the TLV center. Hence, the peak of $\langle u_\theta'^2 \rangle$ there must involve transport and/or inter-component transfer.

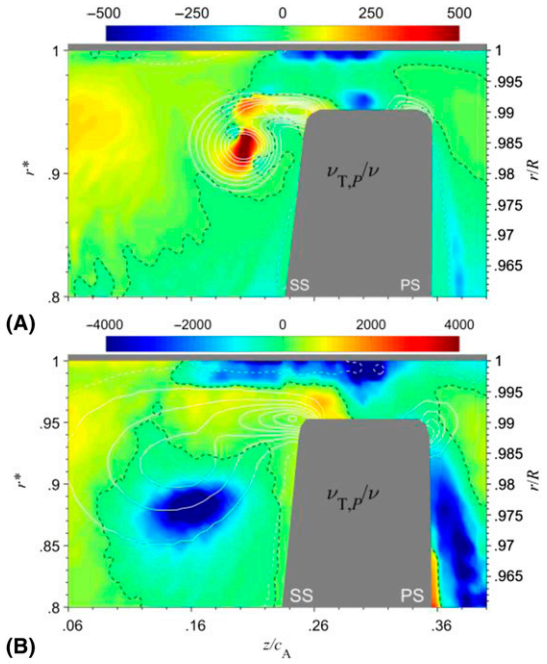

Fig. 9 Sample distributions of eddy viscosity ($\nu_{T,P}/\nu$) estimated using production rate for the axial compressor at (A) $\varphi = .35$ and (B) $\varphi = .25$. The black dashed lines indicate the locations of zero values. The white contour lines correspond to $\langle \omega_\theta \rangle / \Omega$

3.3. Trends of the eddy viscosity and related modeling issues

The experimental data can be used to evaluate the applicability of popular Reynolds stress models to turbomachinery flows. The eddy viscosity concept used extensively in RANS solvers relates the deviatoric Reynolds stresses to the mean strain rates via

$$-\langle u_i' u_j' \rangle + \frac{2}{3} k \delta_{ij} = 2\nu_T S_{ij}. \tag{6}$$

The values of ν_T can be calculated for each stress component or from the overall TKE production rate. Figure 9 shows sample distributions of $\nu_{T,P} = P/(2S_{ij}S_{ij})$ (Soranna et al. 2008) normalized by the kinematic viscosity (ν) for the compressor with a wide gap at two flow rates. As is evident, $\nu_{T,P}$ varies substantially in both sign and magnitude. Negative values, corresponding to $P < 0$, can be observed in broad areas, such as the tip gap, the PS, and under the TLV center. Positive values appear upstream of the TLV, in the shear layer, and near the vortex center at a high flow rate. Furthermore, the misalignment between the Reynolds stress and mean strain rate tensors can be demonstrated by comparing the trends obtained for different components. Sample results for the AxWJ-2 pump are provided in Fig. 10. The mean strain rate is shown in the first row, the corresponding stress is presented in the middle row, and the eddy viscosity calculated from their ratio is provided in the third row. As is evident, the results display extreme variability, and inconsistency in magnitudes and spatial distributions. Similar variabilities have been observed in the compressor (Li et al. 2017). This lack of functional correlation between the Reynolds stress and mean strain rate tensors is a clear manifestation of the non-equilibrium conditions in the tip region of axial turbomachines.

However, despite the disagreement in trends of ν_T for different stress components, results for the same component obtained in

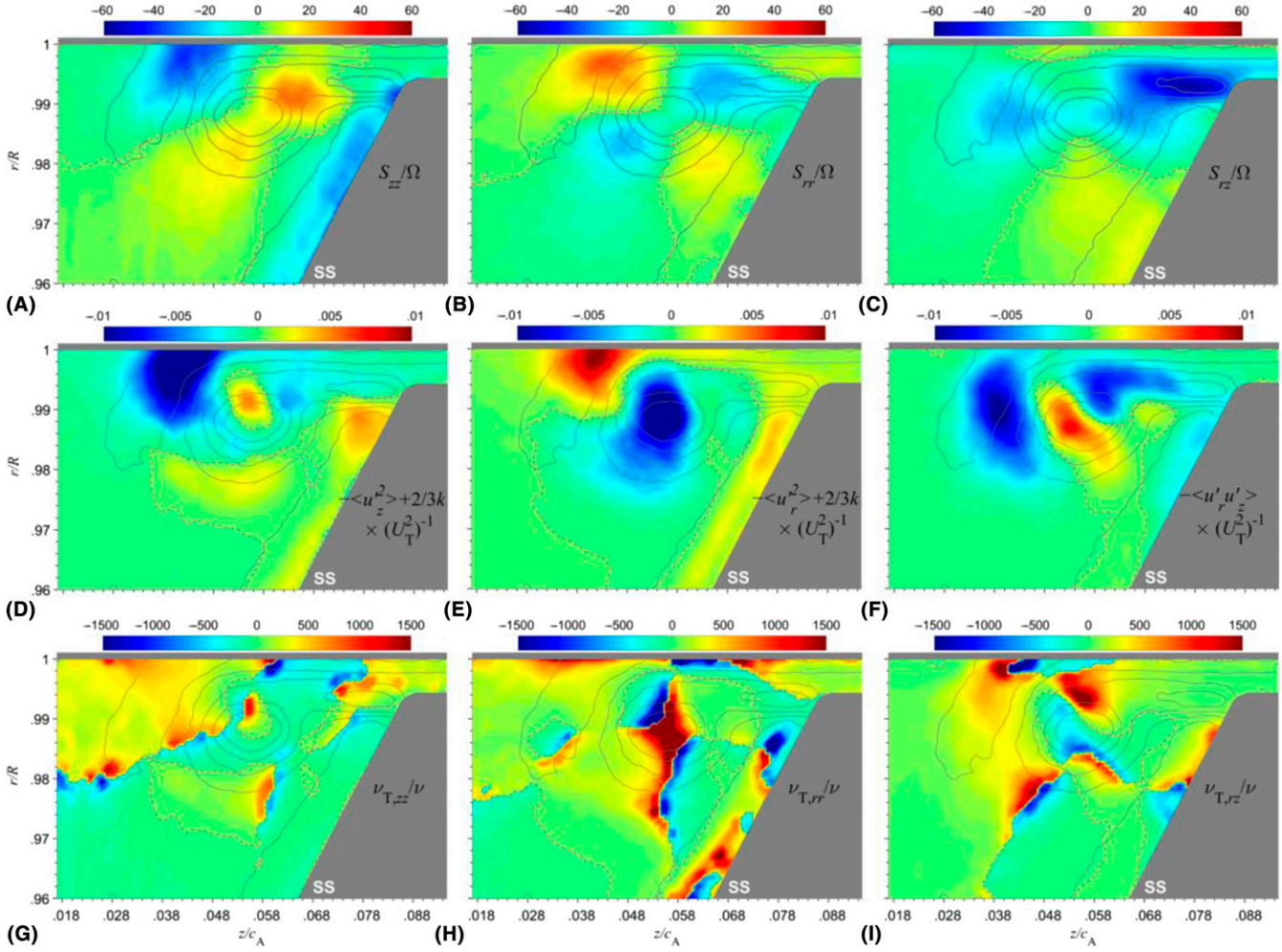

Fig. 10 Sample distributions of (top row) mean strain rate components, (middle row) Reynolds stresses, and (bottom row) corresponding eddy viscosity for the AxWJ-2 pump: (A) S_{zz}/Ω, (B) S_{rr}/Ω, (C) S_{rz}/Ω, (D) $(-\langle u_z'^2\rangle + 2/3k) \times U_T^{-2}$, (E) $(-\langle u_r'^2\rangle + 2/3k) \times U_T^{-2}$, (F) $-\langle u_r' u_z'\rangle \times U_T^{-2}$, (G) $\nu_{T,zz}/\nu$, (H) $\nu_{T,rr}/\nu$, and (I) $\nu_{T,rz}/\nu$. The red dashed lines indicate the locations of zero values. The gray contour lines correspond to $\langle\omega_\theta\rangle/\Omega$

different machines and conditions appear to have similar spatial patterns. As an example, Fig. 11 compares the distributions of the mean shear strain rate S_{rz} (upper row), the corresponding Reynolds shear stress $-<u_r' u_z'>$ (middle row), and the resulting eddy viscosity ν_{rz} (bottom row) for different cases. Corresponding results for the AxWJ-2 pump can be found in Figs. 10C, F, I. In all the distributions, S_{rz} has a clear four-quadrant pattern near the TLV centers, along with large negative values in the shear layers. The shear stress is for the most part negative in the shear layer, the upper (radially outward) half of the TLV center, and in the endwall separated region. In most cases, the stress is positive under the TLV. Consequently, the resulting distributions of eddy viscosity also have similar patterns, e.g., positive values in the middle of the sample area covering the TLV and the shear layer, and negative values below. These common patterns suggest that one might be able to introduce/develop data-based Reynolds stress models that would be applicable to a variety of axial turbomachines, which are based on the mean flow parameters. However, in view of the variability evident in Fig. 10, different models will have to be developed for each of the stress components. As an alternative approach, the broad areas with negative eddy viscosity and the ubiquitous differences between the stresses and their corresponding production rates indicate that models must account for the time history of the stress development as the flow passes through the spatially non-uniform strain field in the rotor passage. A possible approach for the latter might involve implementation of the full Reynolds stress transport models (RSM), which account for the production, transport, and dissipation rates as well as proper models for the effect of pressure. As demonstrated in Liu et al. (2008), RSM can yield more reasonable stress predictions than eddy viscosity–based models for flow in the tip region. Uzol et al. (2007) show that RSM provides better predictions for the evolution of turbulence, at least at mid-span.

4. Conclusions

Measurements of mean flow and Reynolds stresses performed in several axial turbomachines in the JHU refractive index–matched facility reveal several common features in the structure of turbulence in the rotor blade tip region. The mean flow features consist of

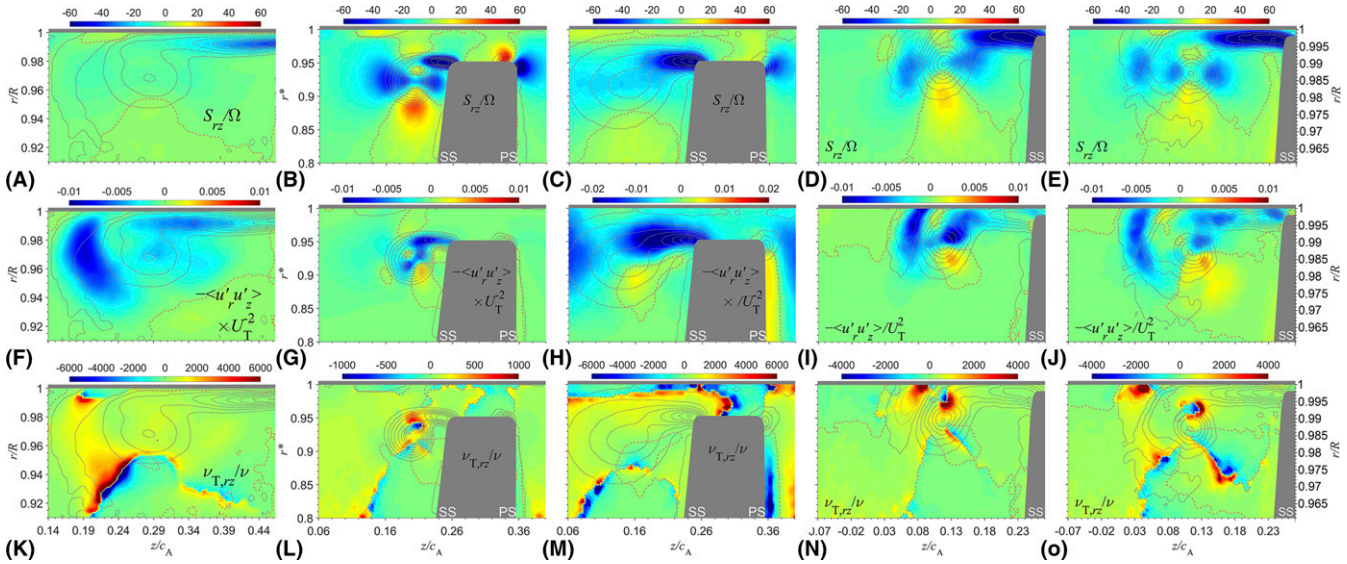

Fig. 11 Sample distributions of (top row) mean shear strain rate S_{rz}/Ω, (middle row) Reynolds shear stress $-\langle u_r' u_z' \rangle \times U_T^{-2}$, and (bottom row) corresponding eddy viscosity $\nu_{T,rz}/\nu$ for (A, F, K) the AxWJ-1 pump, and for the axial compressor with a wide tip gap at (B, G, L) $\varphi = .35$ and (C, H, M) $\varphi = .25$, and with a narrow tip gap at (D, I, N) $\varphi = .35$ and (E, J, O) $\varphi = .25$. The red dashed lines indicate the locations of zero values. The gray contour lines correspond to $\langle \omega_\theta \rangle / \Omega$

several vortical structures, including the TLV, the shear layer between the TLV and the blade SS tip corner, and the separated endwall boundary layer with opposite sign vorticity. Instantaneous realizations show that each of these regions contains multiple vortices with varying strength and location, which contribute significantly to the local turbulence level.

In general, the turbulence in the tip region is highly anisotropic and spatially inhomogeneous. The local distributions of TKE, and normal and shear stresses are compared with those of the corresponding production rates and, in some of the cases, also to the transport terms. The present data do not have sufficient resolution for measuring the dissipation rate, but it is inferred from the balance of the other components. In some areas, trends in the distributions of production rate and stress agree, but in others they do not, indicating that the turbulence is generated in other areas or transferred from other components. For example, the present results provide clear evidence of turbulence ingestion across the tip gap under pre-stall condition and in a machine with a wide gap. The stress-production disagreement is common around the TLV center, where the turbulence is typically high and the production rate is low, or even negative in some cases, leading to the conclusion that the dissipation rate is low there. The primary local sources of turbulence, where the production rate is high, are concentrated in the shear layer and in the separated endwall boundary layer. The primary mechanistic contributors include axial contraction $(-\langle u_z'^2 \rangle S_{zz})$, radial contraction $(-\langle u_r'^2 \rangle S_{rr})$, and shear production $(-2\langle u_z' u_r' \rangle S_{rz})$. As expected, the transport terms are high in regions of stress gradients, with the mean advection rate often having an opposite sign and similar magnitude as the production rate. Variations in spatial distributions of stress and strain rate tensors sometimes cause significant variations in the turbulence production rates. For example, the P is high near the TLV center at $\varphi = .35$ but low at $\varphi = .25$ (Figs. 5A, B). Although there are other effects, the primary reason for the differences between them is associated with P_{zz}^*, in particular the shear production term $-2\langle u_r' u_z' \rangle \partial \langle u_z \rangle / \partial r$. As Figs. 11G, H show, in both cases, the vicinity of the vortex center is characterized by variations in the sign and magnitude of $-\langle u_r' u_z' \rangle$. Although the distributions have some similarities, near the TLV center, the shear stress is negative at $\varphi = .35$ and nearly zero at $\varphi = .25$. Hence, $P_{zz}^* > 0$ at $\varphi = .35$ (Fig. 7D) and very small at $\varphi = .25$ (Fig. 8C). Furthermore, Figs. 8C, F show that at $\varphi = .25$, the low P_{rr}^* and P_{zz}^* have similar magnitudes and opposite signs. Hence, they cancel each other. Conversely, at $\varphi = .35$, P_{rr}^* is still low, but P_{zz}^* is significant (Figs. 7D, H).

Inherent to the non-equilibrium conditions ubiquitous in the tip region, the local Reynolds stresses do not correlate well with the corresponding mean strain rate components. In fact, the measured eddy viscosity is negative over large parts of the tip region. Furthermore, the distributions of eddy viscosity vary substantially among stress/strain components in both sign and magnitude. By contrast, for the same stress/strain, the distributions measured in several machines and under varying conditions appear to be quite similar, introducing the possibility of development of data-based models with broad applications. Another plausible approach might involve the full RSM, where the time evolution of stresses is accounted for.

Acknowledgments

The projects are funded in part by NASA under grant number NNX11AI21A and in part by ONR under grant number N00014-09-1-0353. The authors would like to thank Chunill Hah and Michael Hathaway from NASA Glenn for their guidance and for modifying the LSAC blade geometries to satisfy the constraints of the JHU refractive index–matched facility. We would also like to express our gratitude to Yury Ronzhes for designing all the mechanical parts for all the tested axial turbomachines.

References

Charonko, J. J., King, C. V., Smith, B. L., and Vlachos, P. P. 2010 Assessment of pressure field calculations from particle image velocimetry measurements, *Measurement Science and Technology*, **21**(10), 105401.

Chen, H., Li, Y., Tan, D., and Katz, J. 2017 Visualizations of flow structures in the rotor passage of an axial compressor at the onset of stall, *Journal of Turbomachinery*, **139**(4), 041008.

de Kat, R. and Ganapathisubramani, B. 2013 Pressure from particle image velocimetry for convective flows: A Taylor's hypothesis approach, *Measurement Science and Technology*, **24**(2), 024002.

Delafosse, A., Collignon, M. L., Crine, M., and Toye, D. 2011 Estimation of the turbulent kinetic energy dissipation rate from 2D-PIV measurements in a vessel stirred by an axial mixel TTP impeller, *Chemical Engineering Science*, **66**(8), 1728–1737.

Denton, J. D. 1997 Lessons from rotor 37, *Journal of Thermal Science*, **6**(1), 1–13.

Denton, J. D. 2010 Some limitations of turbomachinery CFD, *Proceedings*, ASME Turbo Expo 2010: Power for Land, Sea, and Air Volume 7: Turbomachinery, Parts A, B, and C (ASME Paper No. GT2010-22540), June 14–18, Glasgow, UK, ASME, 735–745.

Durbin, P. A. 1996 On the K-3 stagnation point anomaly, *International Journal of Heat and Fluid Flow*, **17**(1), 89–90.

Goto, A. 1992 Three-dimensional flow and mixing in an axial flow compressor with different rotor tip clearances, *Journal of Turbomachinery*, **114**(3), 675–685.

Hah, C., Hathaway, M., and Katz, J. 2014 Investigation of unsteady flow field in a low-speed one and a half stage axial compressor, part 2: Effects of tip gap size on the tip clearance flow structure at near stall operation, *Proceedings*, ASME Turbo Expo 2014: Turbine Technical Conference and Exposition Volume 2D: Turbomachinery (GT2014-27094), June 16–20, Düsseldorf, Germany.

Hah, C., Hathaway, M., Katz, J., and Tan, D. 2015 Investigation of unsteady tip clearance flow in a low-speed one and half stage axial compressor with LES and PIV, *Proceedings*, ASME/JSME/KSME 2015 Joint Fluids Engineering Conference Volume 1: Symposia (AJK2015-02061), July 26–31, Seoul, South Korea.

Horlock, J. H. and Denton, J. D. 2005 A review of some early design practice using computational fluid dynamics and a current perspective, *Journal of Turbomachinery*, **127**(1), 5–13.

Inoue, M. and Kuroumaru, M. 1989 Structure of tip clearance flow in an isolated axial compressor rotor, *Journal of Turbomachinery*, **111**(3), 250–256.

Jang, C.-M., Sato, D., and Fukano, T. 2005 Experimental analysis on tip leakage and wake flow in an axial flow fan according to flow rates, *Journal of Fluids Engineering*, **127**(2), 322.

Lakshminarayana, B. 1986 Turbulence modeling for complex shear flows, *AIAA Journal*, **24**(12), 1900–1917.

Lakshminarayana, B. 1996 *Fluid Dynamics and Heat Transfer of Turbomachinery*, New York, NY: John Wiley & Sons, Inc.

Lakshminarayana, B., Davino, R., and Pouagare, M. 1982 Three-dimensional flow field in the tip region of a compressor rotor passage—Part II: Turbulence properties, *Journal of Engineering for Power*, **104**(4), 772–781.

Li, Y., Chen, H., and Katz, J. 2017 Measurements and characterization of turbulence in the tip region of an axial compressor rotor, *Journal of Turbomachinery*, **139**(12), 121003.

Li, Y., Chen, H., Tan, D., and Katz, J. 2016 Effects of tip clearance and operating conditions on the flow structure and turbulence within an axial compressor rotor passage, *Proceedings*, ASME Turbo Expo 2016 (GT201657050), June 13–17, Seoul, South Korea.

Liu, X. and Katz, J. 2006 Instantaneous pressure and material acceleration measurements using a four exposure PIV system, *Experiments in Fluids*, **41**(2), 227–240.

Liu, X. and Katz, J. 2013 Vortex-Corner interactions in a cavity shear layer elucidated by time-resolved measurements of the pressure field, *Journal of Fluid Mechanics*, **728**, 417–457.

Liu, Y., Yu, X., and Liu, B. 2008 Turbulence models assessment for large-scale tip vortices in an axial compressor rotor, *Journal of Propulsion and Power*, **24**(1), 15–25.

Luznik, L., Gurka, R., Nimmo-Smith, W. A. M., Zhu, W., Katz, J., and Osborn, T. R. 2007 Distribution of energy spectra, Reynolds stresses, turbulence production, and dissipation in a tidally driven bottom boundary layer, *Journal of Physical Oceanography*, **37**(6), 1527–1550.

Miorini, R. L., Wu, H., and Katz, J. 2012 The internal structure of the tip leakage vortex within the rotor of an axial waterjet pump, *Journal of Turbomachinery*, **134**(3), 031018.

Moore, J. G. and Moore, J. 1999 Realizability in turbulence modelling for turbomachinery CFD, *Proceedings*, ASME 1999 International Gas Turbine and Aeroengine Congress and Exhibition Volume 1: Aircraft Engine; Marine; Turbomachinery; Microturbines and Small Turbomachinery (99-GT024), June 7–10, Indianapolis, Indiana, V001T03A003.

Peacock, R. E. 1983 A review of turbomachinery tip gap effects part 2: Rotating machinery, *International Journal of Heat and Fluid Flow*, **4**(1), 3–16.

Pope, S. B. 2000 *Turbulent Flows*, 1st ed, UK: Cambridge University Press.

Roth, G. I. and Katz, J. 2001 Five techniques for increasing the speed and accuracy of PIV interrogation, *Measurement Science and Technology*, **12**(3), 238–245.

Soranna, F., Chow, Y.-C., Uzol, O., and Katz, J. 2006 The effect of inlet guide vanes wake impigement on the flow structure and turbulence around a rotor blade, *Journal of Turbomachinery*, **128**(1), 82–95.

Soranna, F., Chow, Y.-C., Uzol, O., and Katz, J. 2008 Turbulence within a turbomachine rotor wake subject to nonuniform contraction, *AIAA Journal*, **46**(11), 2687–2702.

Soranna, F., Chow, Y.-C., Uzol, O., and Katz, J. 2010 The effect of inlet guide vane-wake impingement on the boundary layer and the near-wake of a rotor blade, *Journal of Turbomachinery*, **132**(4), 041016.

Tan, D., Li, Y., Wilkes, I., Miorini, R. L., and Katz, J. 2014 PIV measurements of the flow in the tip region of a compressor rotor, *Proceedings*, ASME 2014 4th Joint US European Fluids Engineering Division Summer Meeting collocated with the ASME 2014 12th International Conference on Nanochannels, Microchannels, and Minichannels. Volume 1B, Symposia: (FEDSM2014-21593), August 3–7, Chicago, Illinois, V01BT10A031.

Tan, D., Li, Y., Wilkes, I., Miorini, R. L., and Katz, J. 2015a Visualization and time-resolved particle image velocimetry measurements of the flow in the tip region of a subsonic compressor rotor, *Journal of Turbomachinery*, **137**(4), 041007.

Tan, D., Li, Y., Wilkes, I., Vagnoni, E., Miorini, R. L., and Katz, J. 2015b Experimental investigation of the role of large scale cavitating vortical structures in performance breakdown of an axial waterjet pump, *Journal of Fluids Engineering*, **137**(11), 111301.

Uzol, O., Brzozowski, D., Chow, Y.-C., Katz, J., and Meneveau, C. 2007 A database of PIV measurements within a turbomachinery stage and sample comparisons with unsteady RANS, *Journal of Turbulence*, **8**, N10.

Wieneke, B. 2005 Stereo-PIV using self-calibration on particle images, *Experiments in Fluids*, **39**(2), 267–280.

Wu, H., Miorini, R. L., and Katz, J. 2011a Measurements of the tip leakage vortex structures and turbulence in the meridional plane of an axial water-jet pump, *Experiments in Fluids*, **50**(4), 989–1003.

Wu, H., Miorini, R. L., Tan, D., and Katz, J. 2011 Turbulence within the tip-leakage vortex of an axial waterjet pump, *AIAA Journal*, **50**(11), 2574–2587.

Wu, H., Tan, D., Miorini, R. L., and Katz, J. 2011b Three dimensional flow structures and associated turbulence in the tip region of a waterjet pump rotor blade, *Experiments in Fluids*, **51**(6), 1721–1737.

Xu, D. and Chen, J. 2013 Accurate estimate of turbulent dissipation rate using PIV data, *Experimental Thermal and Fluid Science*, **44**, 662–672.

Yu, X. J. and Liu, B. J. 2007 Stereoscopic PIV measurement of unsteady flows in an axial compressor stage, *Experimental Thermal and Fluid Science*, **31**(8), 1049–1060.

Zhang, C., Wang, J., Blake, W., and Katz, J. 2017 Deformation of a compliant wall in a turbulent channel flow, *Journal of Fluid Mechanics*, **823**, 345–390.